

# Austenitizing Temperature Effects on the Martensitic Transformation and its Influence on Simulated Welding Residual Stresses in a Microalloyed-Steel

Salvatore Giuliano Peixoto Tropia de Abreu<sup>a</sup>, Rodrigo Rangel Porcaro<sup>a,\*</sup> , Geraldo Lúcio de Faria<sup>a</sup>,  
Leonardo Barbosa Godefroid<sup>a</sup> , Igor Cezar Pereira<sup>b</sup>, Samuel da Silva de Souza<sup>c</sup>

<sup>a</sup>Universidade Federal de Ouro Preto (UFOP), Rede Temática em Engenharia de Materiais (REDEMAT), Ouro Preto, MG, Brasil.

<sup>b</sup>Universidade Federal de Ouro Preto (UFOP), Programa de Pós-Graduação em Engenharia Mecânica (PROPEM), Ouro Preto, MG, Brasil.

<sup>c</sup>Universidade de São Paulo (USP), Pós Graduação em Engenharia de Produtos (PMT), São Paulo, SP, Brasil.

Received: December 30, 2022; Revised: March 16, 2023; Accepted: April 02, 2023

This study focused on the effects of different peak (austenitizing) temperatures ( $T_p$ ) over the martensite start temperature ( $M_s$ ) and its influence on the final residual stresses after welding simulation. For this purpose, the expansion coefficients obtained through physical (dilatometric) simulations of a high-strength low-alloy steel were considered for three peak temperatures: 1300 °C, 1150 °C, and 920 °C and a cooling rate of 25 °C/s. Aiming at clarifying the physical phenomenon behind GTAW welding, one carried out nonlinear transient thermomechanical finite-element (FE) analyses to reconstitute the welding process and simulate the subsequent formation of residual stresses in the HAZ. Once the heat source simulation was calibrated, four material models were created, one for each  $T_p$ , and a fourth model considering a constant expansion coefficient, without considering the martensite transformation for comparison. A Three-bar model was evaluated to isolate the effects of  $T_p$  ( $M_s$ ) in the residual stresses. A composite plate model was also considered, in which the sheet HAZ was subdivided according to the reached peak temperature, and the respective material models were applied. The results show the importance of martensite transformation on the welding-induced residual stress and a clear trend of decreasing tensions with lowering the  $T_p$ , especially over HAZ.

**Keywords:** Austenitizing temperature, Martensite start temperature, Welding-induced residual stress, Numerical simulation, Dilatometry.

## 1. Introduction

Residual stresses are considered mechanical consequences inherent to thermal cycles and temperature gradients imposed on metals during welding<sup>1</sup>. The classic Three-bar model is the most didactic way to understand the development of residual stresses during and after welding<sup>1-3</sup>. However, despite its simplicity, this model is rarely explored in numerical/computational simulation studies<sup>4</sup>.

With the evolution of commercial packages and the improvement of computing capacity over the last decades, numerical simulation has been increasingly applied to predict complex or multi-physics phenomena related to welding<sup>5</sup>. With these advances, most models focus on estimating thermal cycles and the consequent phase transformations, residual stress analysis, and weld pool dynamics, among others. Still, it must be considered that welding-related problems are complex by nature<sup>2</sup>, which requires simplifications/considerations from Engineers or Researchers who develop numerical analyses. Deng and Murakawa<sup>6</sup>, for example, explain the strategy of avoiding the molten pool simulation

in numerical analyses aimed at calculating the temperature fields. To compensate for the effects of convection in the pool on heat transfer, authors generally use a heat transfer coefficient multiplied by 2 or 3 times at temperatures above that corresponding to the melting of the alloy<sup>6</sup>.

Welding simulations that aim to estimate the residual stress fields need to take into account the thermal properties of the material (conductivity, specific heat, and latent heat), the mechanical properties (modulus of elasticity, Poisson's ratio, yield strength, and plasticity) and the density, as a function of temperature<sup>6-8</sup>. The thermal expansion coefficient values are fundamental for estimating the residual stress fields in welding simulations. In the case of transformable materials, such as high-strength and low-alloy steels, solid-state phase transformations and their corresponding influence on the thermal expansion coefficient significantly affect residual stresses' final results<sup>9-11</sup>.

The martensitic transformation can be present in the HAZ of several structural steels due to the relatively high cooling rates obtained after welding<sup>2,12</sup>. It is known that the HAZ is subdivided according to the peak temperatures ( $T_p$ ) reached in each region and the consequent physical metallurgy

\*e-mail: [rodrigo.porcaro@ufop.edu.br](mailto:rodrigo.porcaro@ufop.edu.br)

phenomena that can occur, for example, austenitic grain growth, precipitate dissolution, recovery/recrystallization and the resultant phase transformations in the post-welding solid state<sup>1,2</sup>. Some simulation works have explored the effects of the martensitic transformation on the residual stress in welding<sup>13-15</sup>, including the development of filler metals aiming to reduce the level of residual stresses from the formation of martensite, being the martensite-start temperature ( $M_s$ ) a relevant factor<sup>16</sup>. However, the  $M_s$  values are not fixed for a given material, and, in the case of HAZ, the peak temperature can significantly influence this parameter<sup>12</sup>.

In a previous work<sup>12</sup>, the effects of austenitization temperature on grain size and martensitic transformation kinetics were explored for microalloyed steel. The authors showed that the increase in the austenitization temperature significantly modified the  $M_s$  temperature and emphasized that, most likely, these differences along the HAZ could be relevant for welding simulation<sup>12</sup>.

In this context, the effects of the austenitization temperature on  $M_s$  and its consequences on the field of residual stresses in welding were estimated from numerical computational simulations with the aid of Ansys<sup>®</sup> Software. Three-bar models were developed to isolate the effects of the martensitic transformation. A butt joint welding model was also produced and validated with a physical model using thermocouples. From this model, the effects of considering or not the martensitic transformation on residual stresses were evaluated, as well as the effects of different peak temperatures, with a subdivision of the HAZ and its influence

on the residual stress results. The subdivision of the HAZ and the evaluation of the effects of  $T_p$  on the  $M_s$  temperature as well as the consequent effects on the residual stresses is an unprecedented approach in the technical literature.

## 2. Materials and Methods

### 2.1 Material

The thermal expansion data, considering the martensitic transformation, used in the numerical simulations were obtained from a low carbon steel studied by<sup>12,17</sup>, whose chemical composition can be seen in Table 1. In its composition, one can see the presence of alloying elements such as Mn, Cr, Mo, and Ti, which increase the hardenability when under continuous cooling. The data in question were obtained considering three  $T_p$ , 920 °C, 1150 °C, and 1300 °C, with a cooling rate of 25 °C/s, determined as the critical rate for the total martensitic transformation in the evaluated material<sup>12,17</sup>. The thermal expansion data, as a function of temperature for the different  $T_p$ , were measured in dilatometry tests in a cooling regime and treated with the aid of the Origin<sup>®</sup> Software.

Figure 1a illustrates a dilatometric curve obtained with an austenitization temperature ( $T_p$ ) equal to 920 °C and a cooling rate of 25 °C/s. The  $de/dT$  values on the curve represent the instantaneous coefficient of thermal expansion. It can be seen that during the martensitic transformation, the expansion coefficient assumes negative values, which represents the

**Table 1.** Chemical composition of the studied steel (wt.%)<sup>12,17</sup>.

C	Si	Mn	P	S	Cr	Mo	Nb	Ti	V	N
0.1	0.3	0.9	0.02	0.003	0.7	0.5	0.005	0.02	0.04	0.005

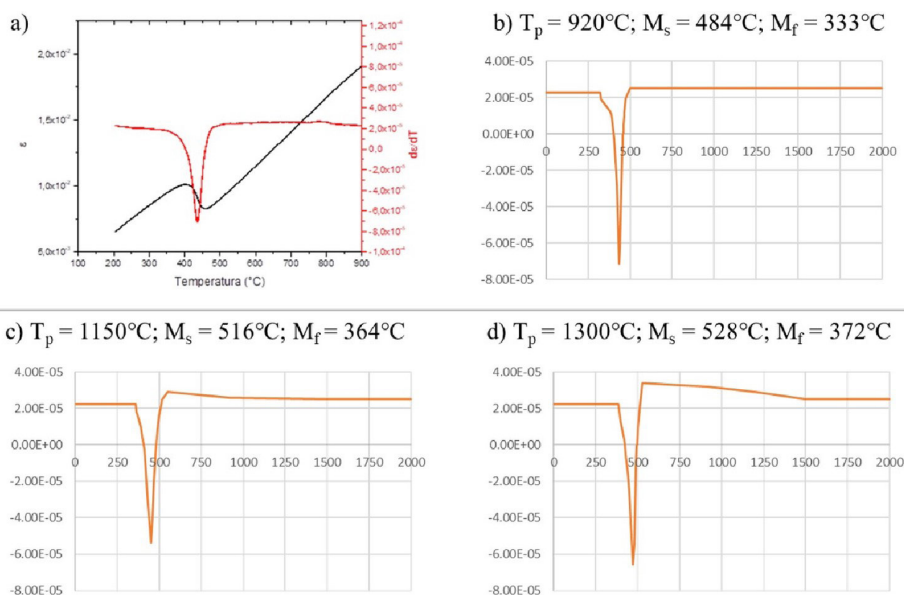


**Figure 1.** a) Dilatometric data of the steel with  $T_p$  of 920 °C and cooling rate of 25 °C/s; b) Simplified expansion coefficient curve for  $T_p$  920 °C cooling rate of 25 °C/s; c) Expansion coefficient curve for  $T_p$  1150 °C cooling rate of 25 °C/s; d) Expansion coefficient curve for  $T_p$  1300 °C cooling rate of 25 °C/s, according with Souza<sup>17</sup>.

thermal expansion associated with the martensitic phase transformation. The thermal expansion coefficient values were obtained for the different  $T_p$ 's evaluated in this work, and the data were simplified to a total of 20 to 30 points (depending on the austenitization temperature) for inclusion in the materials model in the software, Figure 1b, 1c, and 1d. As can be seen, the peak temperature has a significant influence on the temperatures of the beginning and end of the martensitic transformation<sup>12,17</sup>, a fact that is not generally taken into account in the simulations of welding-induced residual stresses<sup>6,8,11,18,19</sup>. According to Deng<sup>12</sup> and Souza<sup>17</sup>, the peak temperature applied to the material can influence the  $M_s$  values in two main ways. The first is linked to the dissolution of precipitated carbides and nitrides, causing a change in the chemical composition of austenite. Due to this effect, there is a change in chemical energy, facilitating the martensitic transformation at higher temperatures. The second main cause is related to the austenitic grain size motivated by the higher  $T_p$ . On this occasion, the energy required to accommodate the volumetric expansion resulting from the martensitic transformation increases with decreasing austenitic grain size.

## 2.2 Welding procedure

The welding process chosen for butt welding and its subsequent numerical simulations was GTAW, mainly due to the easier control of the variables and the absence of filler metal. These characteristics help in its numerical modeling, thus requiring fewer approximations and considerations, keeping the model more faithful to the actual process.

The welding procedure was carried out on a low carbon steel plate measuring 250x200x3 mm, in which a weld pass was made with an approximate length of 150 mm, starting with a distance of 50 mm from the edge, direct current with negative electrode of 115 A, a voltage of 10 V, and torch movement speed of 2.5 mm/s and shielding with argon gas.

The mechanical device developed and described in Tavares et al.<sup>20</sup> was used to obtain a mechanized weld to eliminate human factors that could affect the results. Through this, it was possible to maintain fine control over the torch's angulation, alignment, welding speed, and arc length.

## 2.3 Experimental Acquisition of Temperatures for the Heat Source Validation

Aiming to calibrate the computational thermal model, three type-K thermocouples were resistance welded on the plate before the GTAW welding procedure. With reference to the center line of the plate, the thermocouples were positioned at 10 mm, 15 mm, and 20 mm, with the closest and farthest at the bottom of the plate and the medium at the top, as shown in Figure 2. Thermal cycles at the three points monitored by thermocouples were acquired at 200 ms intervals and used to calibrate and validate the numerical model.

## 2.4 Numerical simulation

Even using the GTAW process, numerical modeling of welding still presents a high complexity, a great challenge for current engineering. Much of the difficulty comes from the sheer number of variables to be considered and the intricate interactions between the fields of temperature, microstructure, and deformation<sup>7,21</sup>.

The temperature field involves the solution of the transient temperature gradient between the heat source and the studied body by conduction. The main boundary conditions to consider are the heat losses by radiation and convection at the body's surface as well as the parameters for the heat source. Covered by the microstructural field are the phase changes undergone by the material because of temperature changes, which are described in the thermomechanical model of the material. Finally, the deformation field is characterized by the calculation of residual stresses resulting from volume changes coming from the material's thermal expansion (temperature field) and phase transformations (microstructural field)<sup>22</sup>. A complete welding simulation would incorporate all interactions between these fields, as shown in Figure 3 and Table 2, as well as complex models for radiation and convection heat losses<sup>7,21-23</sup>.

If the simulations were performed considering each of the interactions described above, simultaneously, the solution would require an unfeasible computational time. Furthermore, some parameters would have a minor or negligible influence on the final result, adding unnecessary

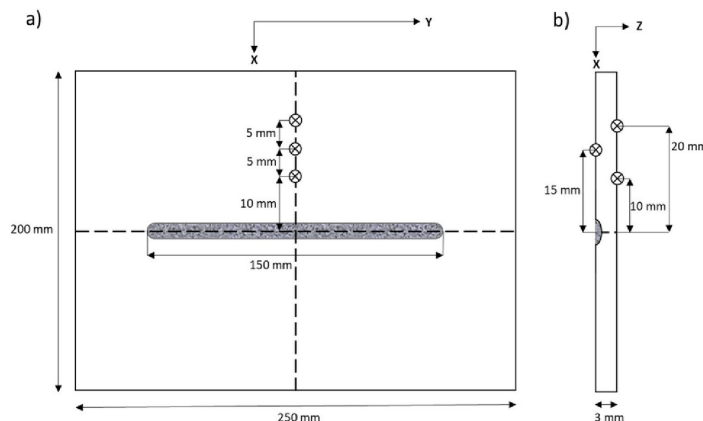


**Figure 2.** Schematic figure presenting the dimensions of the welded plate and relative positions of the thermocouples to the weld bead. a) Top view; b) Side view.

**Table 2.** Relations displayed in Figure 2, according to Knoedel et al.<sup>22</sup> and Lindgren<sup>23</sup>.

Index	Relations
1	Thermal expansion due to the microstructure.
2	Volume changes due to phase transformations.
3	Plastic material behavior is dependent on the microstructure.
4	Elastic material behavior is dependent on the microstructure.
5	Heat loss due to plastic and elastic dissipation.
6	Heat generated by thermal strain.
7	Heat generated by elastic strain.
8	Microstructure evolution is dependent on temperature.
9	Heat conductivity and heat capacity depending on the microstructure.
10	Latent heat due to phase changes.
11	Deformation changes thermal boundary conditions.
12	Deformations caused by temperature changes
13	Microstructure evolution is dependent on deformation.
14	Deformations are from microstructural evolution

complexity<sup>7,13,14,23</sup>. To simplify the problem, some of the interactions are discarded or approximated, and the analysis is chosen to be carried out in two steps. The first is the solution of the thermal field and its history, followed by the solution of the strain field using the results of the first step as thermal load and the microstructural changes embedded in the thermomechanical properties of the material to be studied<sup>7,13,14,18,23</sup>. Figure 4 shows the primary considerations used for the simulation solution<sup>7,23</sup>.

The martensitic transformation brings three mechanisms that interfere with the residual stress, namely: the effect of the material's plasticity that imposes a relaxation on the structure; the increase in the resistance limit of the material; and the volume expansion that counteracts the effect of contraction of the material with the decrease in temperature<sup>9,19</sup>. The last one presents the most significant effects<sup>9,14,19</sup>, being the only one to be considered in this study and one of the main simplifications applied

One of the focuses of this study is to investigate the effects of the  $T_p$  over the  $M_s$ . During the literature review, it was found that, in most of the simulation studies in which the martensitic transformation is considered, a fixed value for  $M_s$  is used. For this, the values of  $M_s$  are usually extracted from a material previously studied or measured for the study<sup>22,24</sup>, obtained by empirical formulas and mathematical models based on chemical composition<sup>13,15,16,25</sup>, or by approximations of similar materials<sup>8,9,14,18</sup>. Nevertheless, this strategy leads to a relatively common approach of ignoring the effects that  $T_p$  brings on  $M_s$  and its subsequent effects on the final residual stresses, something that, as it will be shown in the results of the Three-bar and Plate models, cannot be ignored. Interestingly, Deng<sup>13</sup> considers two  $T_p$  for calculating the martensite fraction present during cooling. However, the author did not implement their effects in the  $M_s$  calculations.

#### 2.4.1 Heat Source calibration

Once the thermocouple temperature profiles were acquired, a model was created to calibrate and validate the

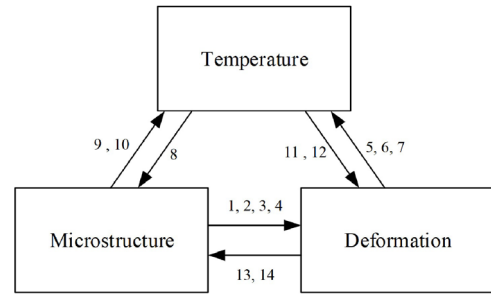


**Figure 3.** Phenomena observed during a weld, according to Knoedel et al.<sup>22</sup> and Lindgren<sup>23</sup>. See Table 2 for the numbered paths.

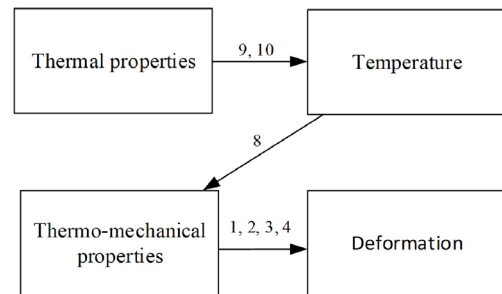


**Figure 4.** Considered phenomena for the thermal-mechanic simulations following simplifications of Figure 3, according to Knoedel et al.<sup>22</sup> and Lindgren<sup>23</sup>.

heat source used in the computational simulations. The model has dimensions of 200x100x3 mm, a size that ensures the complete development of the temperature profile without being influenced by edge effects, as illustrated by Figure 5, having a total of 11760 elements and 55887 nodes. For the comparison of the thermal profiles, monitoring points were added in the model (domain) in positions that are equivalent to the thermocouples used in the real plate.

Following a strategy chosen by<sup>26-28</sup>, due to the relative difficulty of finding models of thermal properties for each specific alloy, it was chosen to use the material properties described by<sup>6</sup>, shown in Figure 6, for an ASTM A36 steel as a basis for the calibration of the thermal model. This material was selected mainly because it has a chemical composition and a microstructure similar to the steel used in this part of the study. Therefore, it is reasonable to assume that, although not identical, both materials should have similar thermal properties.

The focus of this work is not on a detailed characterization of the molten zone but on the analysis of the state of residual stresses distributed throughout the sheet after the welding procedure. Thus, the Gaussian model was selected for the heat source, capable of accurately describing the necessary thermal profiles, mainly for studies with GTAW welding<sup>29,30</sup>. The Gaussian model can be described by Equation 1<sup>29</sup>.

$$q(r) = \frac{\eta UI}{2\pi s^2} e^{-\left(\frac{r^2}{2s^2}\right)} \quad \text{eq 1}$$

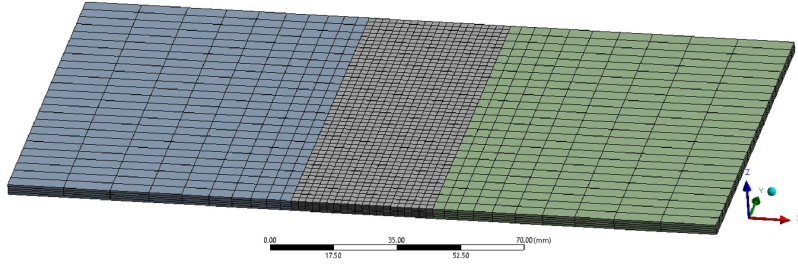


Figure 5. Geometry and mesh used for the thermal calibration.

Where:  $q(r)$  = surface flux for a radius  $r$ ;  $\eta$  = Electric arc efficiency;  $U$  = Voltage;  $s$  = radial distance;  $I$  = Current.

Considering Equation 1, two variables stand out in importance since they are not straightforwardly known: radial distance ( $s$ ) and arc efficiency ( $\eta$ ). The first describes the distribution of heat flux intensity along a circular base of the Gaussian model. The work presented by Araújo et al.<sup>29</sup> demonstrates in detail the influence of the radial distance on the heat distribution on the plate. Studies in the literature<sup>29-31</sup> report arc efficiency values ranging from 0.7 to 0.9 for GTAW welding under conditions similar to those used in this work.

Another essential factor to consider in thermal simulations is the material cooling boundary conditions, specifically the convection and radiation coefficients, respectively, described by Newton's (Equation 2) and Stefan-Boltzman's (Equation 3) heat transfer laws. Literature sources<sup>6,25,29</sup> indicate values between 8 and 30  $W/^\circ C m^2$  for the convection coefficient and between 0.2 and 0.9 for the emissivity.

$$q_c = h_c (T - T_0) \quad \text{eq 2}$$

$$q_r = \epsilon_r \sigma_r (T^4 - T_0^4) \quad \text{eq 3}$$

Where:  $q_c$  = convection heat flux;  $q_r$  = radiation heat flux;  $h_c$  = convection coefficients;  $T$  = surface temperature;  $T_0$  = room temperature;  $\epsilon_r$  = material emissivity constant;  $\sigma_r$  = Stefan-Boltzman constant.

The determination of the values to be used in the simulation of radial distance, arc efficiency, and radiation and convection coefficients was carried out with the aid of the literature and by an iterative process. To this end, case by case, an assessment was made of the thermal cycles resulting from the simulations with those observed after the welding procedure. Data acquired by thermocouples and macrographs transversal to the weld bead were used as comparison parameters, evaluating the dimensions, area, and shape of the limit of the fused zone, whose limit was estimated as a temperature of 1336.6  $^\circ C$ <sup>29</sup>.

#### 2.4.1 Three-bar Model

To initially understand the development of residual stresses after heating/cooling, a set of simulations were performed considering a Three-bar model as explained in Marques et al.<sup>3</sup> and studied by Darmadi<sup>4</sup>. The experiment in question is a theoretical and simplified evaluation of the stress distribution due to expansions and contractions within the material after localized heating/cooling. The Three-bar model

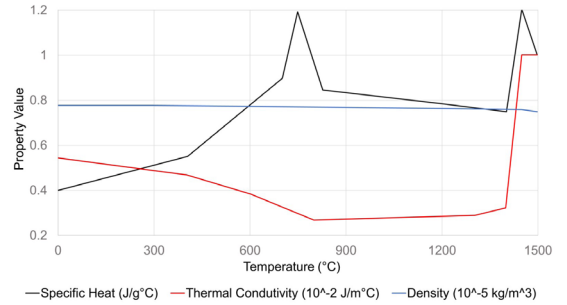


Figure 6. Thermal properties of ASTM A36 steel, according to Deng and Murakawa<sup>6</sup>.

is based on two transverse supports with 100x40x20 mm responsible for restricting the freedom of movement between the three identical vertical cylindrical bars with a 5 mm radius and 100 mm length. To avoid possible errors in the simulation due to a stress concentration (geometric effect), flanges with a 5 mm radius were added to the top and bottom of the bars. In total, the model has 2646 elements and 4005 nodes, as can be seen in Figure 7.

The Three-bar model was built based on the thermal-mechanical material model described by<sup>26</sup>, shown in Figure 8. This model was chosen because it describes high mechanical strength steel whose thermomechanical characteristics are similar to the steel studied by<sup>12,17</sup>. In addition, to this material model were introduced the expansion coefficient data obtained by<sup>17</sup> for  $T_p$  920  $^\circ C$ , 1150  $^\circ C$ , and 1300  $^\circ C$  at a cooling rate of 25  $^\circ C/s$ , visualized in Figure 1b, 1c, and 1d. Creating three new material models, P920, P1150, and P1300, following a strategy similar to Deng<sup>13</sup> and Deng and Murakawa<sup>14</sup>. An extra material model was also created with a constant expansion coefficient equal to  $2.07 \times 10^{-5} \text{ }^\circ C^{-1}$ , as in<sup>17</sup>. The purpose of this new model is to promote the comparison of the final stress states with and without considering the martensitic transformation, referred to as PCTE.

To simulate the thermal aspects, the central bar was divided into three parts, the cylindrical volume and the two regions of the flanges. At the boundary between these regions, thermal insulation condition was stipulated so that the extra surface area of the flanges would not introduce a thermal gradient in the cylindrical region, in addition to preventing the flow of heat to the transverse supports.

For the entire cylindrical volume of the central bar, heating was applied starting from ambient temperature

(22 °C) to a temperature of approximately 1450 °C, following a heating profile observed during the calibration of the heat source, presented as the red line of Figure 7. While from the second 17 s-forward, a cooling condition was applied. For this purpose, a convection coefficient of 475 W/m<sup>2</sup>°C

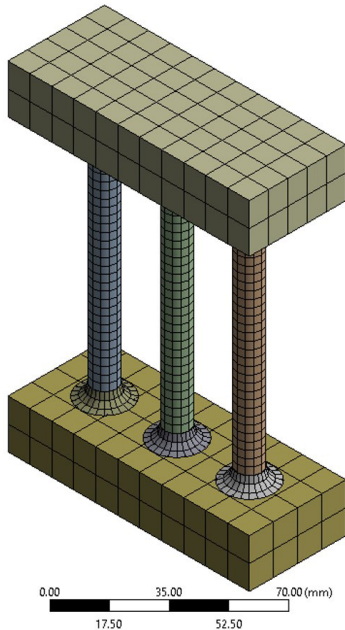


**Figure 7.** Geometry and mesh used in the Three-bar model.

and an emissivity coefficient of 0.8 was used to ensure a cooling rate of 25 °C/s. The resulting cooling is shown by the blue line of the curve in Figure 9.

For the stress analysis, a fixed support was applied to the upper surface of the upper transverse support and the lower surface of the lower transverse support. This condition must be implemented to restrict the model's movement through space (rigid body motion). Finally, due to the inconsistency of the location of the points of the maximum and minimum stresses in the central bar, the results were evaluated by considering the absolute values of the eight most central elements of the middle bar, featured in Figure 10.

#### 2.4.2 Plate model with martensitic transformation

The last set of numerical simulations to be presented in this work consisted of a model with the exact dimensions, boundary conditions, and parameters of the thermal source used to calibrate the heat source. However, the domain (plate) was subdivided considering the peak temperature reached during the simulations, according to the temperatures at which the dilatometric data was acquired, as shown in Figure 11a, to produce a Compound model. The yellow and red areas were combined, and the P1300 material model was assigned, while the turquoise and blue areas were applied to the P1150 and P920 models, respectively. The two most external bodies, with coarser mesh, were assigned the material P920. For comparison purposes, simulations were also conducted considering the entire plate with materials P1300, P1150, P920, and PCTE. In this way, it was possible to evaluate the effects of considering or not the martensitic transformation (thermal expansion) on the residual stress field, in addition to the influence of  $T_p$  on  $M_s$  and, consequently,

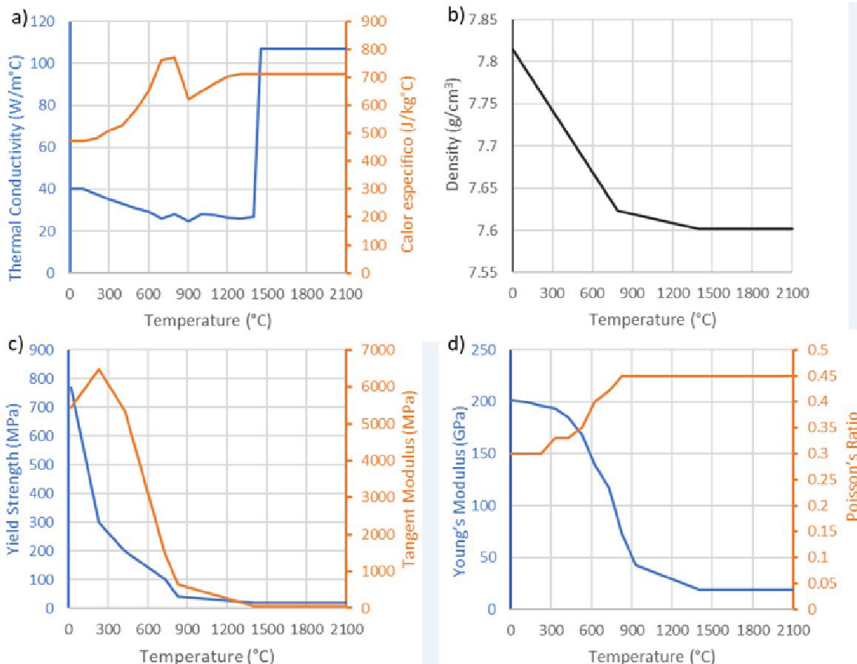


**Figure 8.** Thermo-mechanical properties of the material model a) Thermal Conductivity (W/m°C) and Specific Heat (J/Kg°C); b) Density (g/cm<sup>3</sup>); c) Yield Strength (MPa) and Tangent Modulus (MPa); d) Young's Modulus (GPa) and Poisson's Ratio. According to Porcaro<sup>26</sup>.

on the response of the thermomechanical model. The final model has five bodies which can be seen in Figure 11b, containing 5184 elements and 28299 nodes.

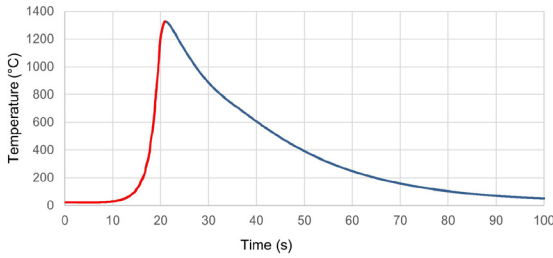


Figure 9. Temperature profile used in the Three-bar model.

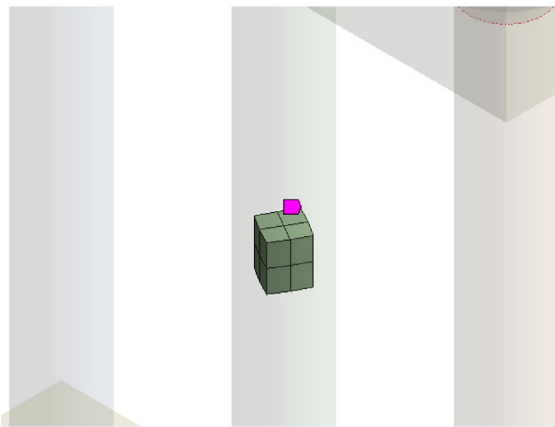


Figure 10. Chosen central elements to monitor the development of stresses in the central bar of the Three-bar model.

With the same objectives of the Three-bar model, for consideration of the mechanical simulations, an immobility condition was applied to the right-side face of the model. The choice to apply this condition between the right and left faces was made arbitrarily, and it should be noted that it did not imply a change in the symmetry of the stresses distributed across the plate.

### 3. Results and Discussion

#### 3.1 Heat Source Calibration

Once the GTAW welding was performed on the test plate, the data from the thermocouples were analyzed and used as a basis for the calibration of the heat source and the emissivity and convection constants. The comparison between the simulated thermal profiles and those obtained through thermocouples can be seen in Figure 12 and Table 3. Generally, a good agreement between peak temperature data and heating and cooling rates is observed.

Along with recording the thermocouples, macrographs were taken in the middle of the weld bead in the perpendicular direction to reveal the shape of the fusion zone. The images of the macrographs and simulations were evaluated using the ImageJ<sup>®</sup> software, and the results of the size of the molten

Table 3. Peak temperature comparison between the experimental and simulated results.

	TC* 10mm (°C)	TC* 15mm (°C)	TC* 20mm (°C)
Simulated	503.11	381.36	305.65
Experimental	489.203	396.678	302.464
Difference (%)	2.84	-3.86	1.05

\*TC thermocouple.

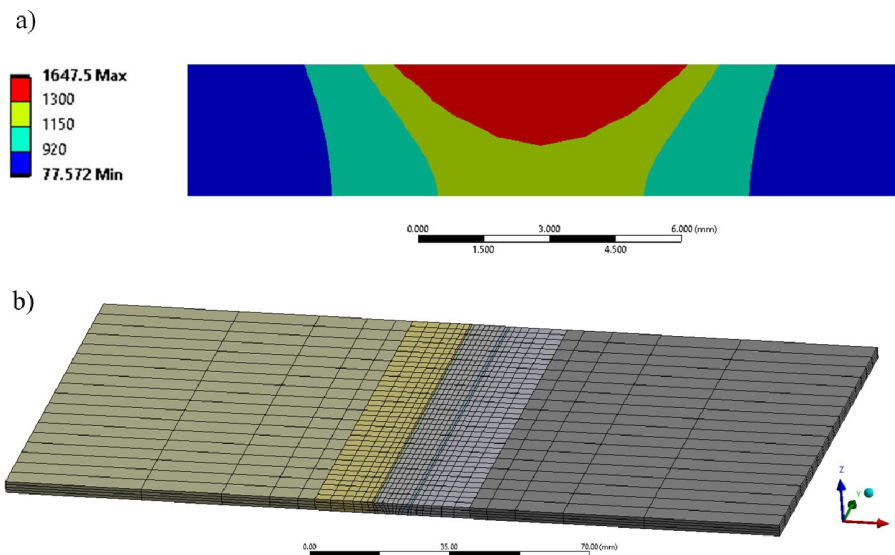
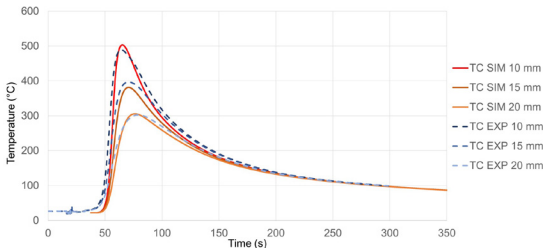


Figure 11. a) Temperature distribution around the ZTA used to delimit the used materials models for the Plate model; b) Final geometry and mesh used in the Plate model.

zone were used to calibrate the heat source model, whose final results can be seen in Figure 13 and Table 4. As considered by<sup>29</sup>, the temperature of 1336 °C was used as the limit for the molten zone, represented by the red line in Figure 13.

After the iterative tests, the thermal boundary conditions were determined as a convection coefficient equal to 10 W/m<sup>2</sup>°C and an emissivity coefficient of 0.8. The heat source parameters considered were an arc efficiency of 0.7 and a radial distance of 3.1 mm. For all variables, the used values are consistent with those observed in the literature<sup>6,25,29</sup>. Figure 14 shows the plate's simulated heating and cooling regimes at various time intervals.



**Figure 12.** Comparison between the experimental and simulated temperature profiles for the three thermocouples TC SIM: Simulated; TC EXP: Experimental-Thermocouple.

### 3.2.1 Three-bar model residual stresses simulation

The next step was to assign the materials PCTE, P920, P1150, and P1300 to the central bar and its respective flanges and carry out the stress simulations. The result of the residual tensile stresses on the Y axis in the most central eight elements of the middle bar can be seen in Figure 15.

In general, it is observed that for all cases of material models, the results are consistent with those obtained in the experiment proposed in<sup>3</sup> and simulated by Darmadi<sup>4</sup>. The central bar initially passes through a state of compression during heating, and with continued cooling (time increase), this stress reverses to a state of tensile stress, which increases in value until the final temperature is reached.

Analyzing the results of each material model, in the PCTE model, the stresses rise to the maximum value of 1288 MPa without interruptions (during cooling). On the other hand, for the models in which the martensitic transformation is

**Table 4.** Comparison between the dimensions of the experimental and simulated results of the fusion zone.

Weld bead dimensions	Simulated	Experimental
Maximum depth	1,970 mm	1,828 mm
Width	6,375 mm	6,18 mm
Area	7,262 mm <sup>2</sup>	7,375 mm <sup>2</sup>

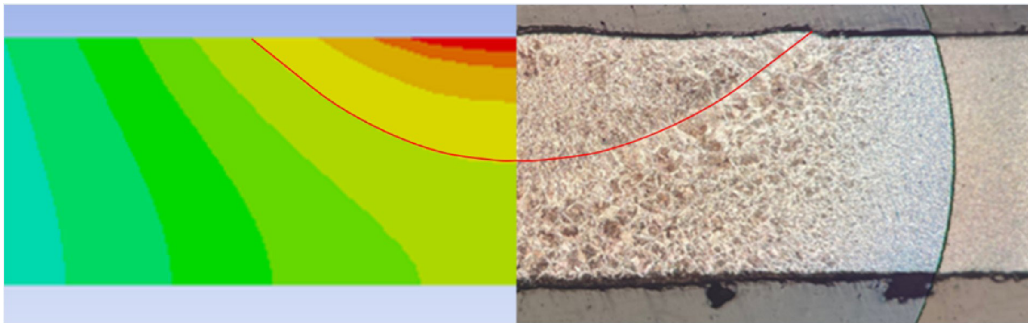


**Figure 13.** Fusion zone shape comparison between simulated and experimental. The red line represents the limit considered for the fusion zone.

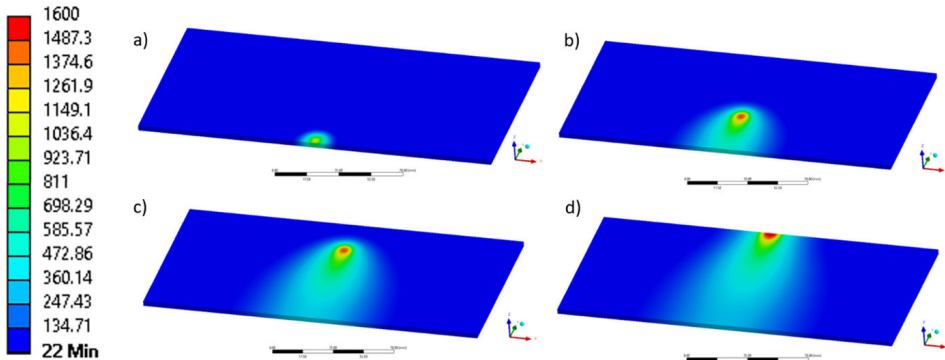


**Figure 14.** Temperature distribution in the heat source calibration model at: a) 1.5 s; b) 15 s; c) 30 s; d) 40 s.

considered, during cooling, “valleys” are observed close to the mark of 40 seconds, which coincide with the temperatures of  $M_s$  and  $M_f$  of each of the materials. These sections act as a temporary stress relief point in the body, resulting in progressively lower values of the final stress with the decrease of  $T_p$  and consequent decrease of the values of  $M_s$ . The final values are 1259, 1196, and 1179.6 MPa, respectively, for the materials P1300, P1150, and P920.

These results reflect the discussion raised by<sup>9</sup>, which shows that if the transformation is completed before the end of cooling, additional contraction may occur, leading to an increase in tensile stress, a fact observed in the simulation results and attributed to the high values of  $M_s$  of the studied steel. Thus, as shown by<sup>9,24</sup> in a study on residual stresses for filler metals with low transformation temperature, materials with lower  $M_s$  may bring greater benefits in reducing residual stresses.

The results of the Three-bar models complement the studies by<sup>11,13,14</sup> reiterating the need to consider phase transformations, especially the martensitic transformation, to accurately describe the post-welding residual stresses in medium carbon steels.

### 3.3 Plate model residual stresses simulation

Figure 16 presents a comparison between the thermal profile of the model obtained by the calibration of the heat source and the result of the Compound model at two points: the first one central to the plate and with a depth of 1.5 mm and a second point at 20 mm to the left. It is possible to observe that both pairs assume similar peak shapes and temperatures. Furthermore, when calculating the cooling rate ( $t_{8-5}$ ) of the Compound Plate model at the center of the top surface, a rate of 24.32 °C/s was obtained, very close to the one used to extract the expansion coefficient data of 25 °C/s in<sup>17</sup>. These two factors reinforce the accuracy of the thermal source model and its possibility of application as a valid heat source for the Compound model. Due to the uncoupled nature of the thermal simulation and the equal thermal properties of the materials P1300, P1150, P920, and PCTE, the thermal results are bound to be the same as the ones observed in the Composite model.

For the analysis of the stress tables for each of the simulated models, a line that crosses the entire width of the model and at a depth of 1.5 mm was chosen as a reference. Analyzing the results, it was noticed that the residual stresses in the z direction (by the thickness of the plate) exhibited low

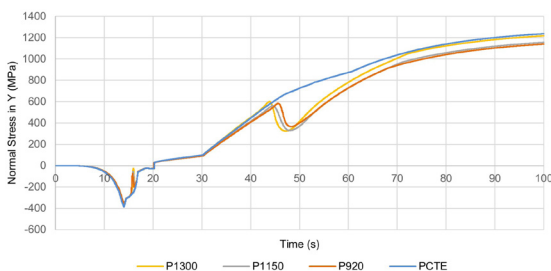


**Figure 15.** Development of the maximum stress value in the middle bar's central elements.

values, not exceeding 15 MPa, being disregarded from the final analysis. Similar results were presented by<sup>25</sup>. Transversal (perpendicular to the weld bead) and longitudinal (parallel to the weld bead) values present much more significant values. Figures 17 and 18 compare the simulated final stress states for each model evaluated for transverse and longitudinal stresses, respectively.

As seen in Figure 17, the stresses of the PCTE material present a distribution similar to that observed in<sup>6,8,10,21,22,30</sup>, in which the curve has a characteristic “M” shape, with relatively lower stresses in the center of the ZF and tensile peaks in the HAZ.

On the other hand, the models with materials P920, P1150, and P1300 showed similar behavior in the stress distribution and their absolute values. The models considering the martensitic transformations, at their peaks, showed a difference of approximately 80 MPa compared to the PCTE model, as expected and shown by<sup>6,8,10,21,22,30</sup>. These cases

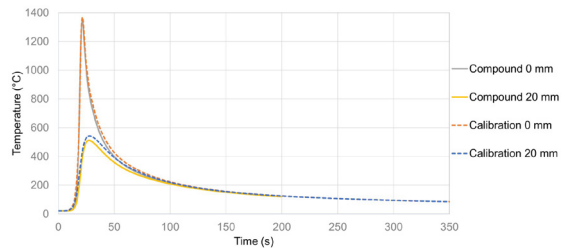


**Figure 16.** Temperature profile comparison between the heat source calibration and Compound Plate models.

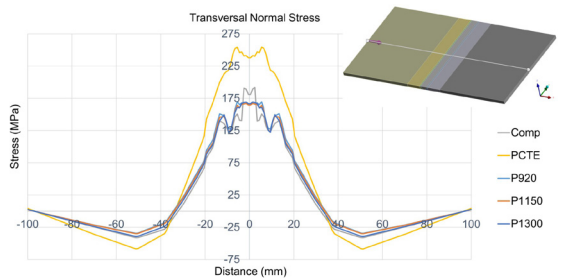


**Figure 17.** Comparison of the transversal residual stresses for all material models.

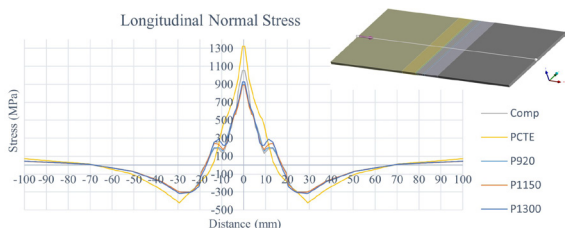


**Figure 18.** Comparison of the longitudinal residual stresses for all material models.

exhibit a stress plateau in the WZ region, followed by a stress relief area located in the HAZ approximately 8 mm from the center line, which occurs at the location whose maximum temperature is between  $M_s$  and  $M_f$ . The compound model presented intermediate stress values between the PCTE and the others and presented three distinct stress relief zones. This interaction is probably related to each material's different stress relief times.

The trends observed for the transverse stresses are repeated for the longitudinal stresses, in which the model with PCTE material presented the most extreme stress states with a difference, at its peak, of approximately 400 MPa above the models in which the martensitic transformation is considered, indicating the importance of this variable for the final results.

The models with martensitic transformation also showed similar behavior to each other; however, the differences between them are more easily observed. The model P1300, which has the highest temperatures of  $M_s$ , presented a difference of approximately 50 MPa and 100 MPa, respectively, at the center of the weld and the HAZ compared to the case with P920 material. While the stress profile of the material P1150 fits almost ideally between the profiles of P1300 and P920, as expected, given their intermediate  $M_s$ . The effects of  $M_s$  can be observed mainly in the HAZ, where stresses are scaling with increasing values of  $T_p$  reaching a difference of approximately 100 MPa between the P1300 and P920 models. In addition, the compound model presents an intermediate stress peak at the center of the plate and the highest stress relief in the HAZ among the models in which the martensitic transformation was considered.

Although the results of longitudinal stresses showed a more accentuated peak in the central region of the plate, in general, the results of residual stresses obtained along the thickness, transversal, and longitudinal directions agree with those observed in the literature<sup>6,8,10,21,22,30</sup>. It should be noted that the simulated stresses in this study were considerably higher than other models observed in the literature. Nevertheless, this can be easily attributed to the higher mechanical strength of the modeled material and high  $M_s$  temperature.

A noteworthy study that considered the effects of  $T_p$  on the final stresses was that of Heinze et al.<sup>32</sup>, in which studies were carried out for two materials, and three  $T_p$  were considered for each. The study shows how the austenitic grain size is influenced by  $T_p$ , triggering changes in the  $M_s$  of the materials and subsequently in the post-weld final stress state. The first material presented a final martensite fraction of only 11%, so the difference in the final stress state between the models that considered and not the influences of  $T_p$  on  $M_s$  could be neglected. On the other hand, the second material showed a complete martensitic transformation, where the influence of the increase of  $T_p$  over the  $M_s$  was more apparent, increasing the final stress in the HAZ of approximately 200 MPa. In general, the results presented by<sup>32</sup> align with those presented by this study since they demonstrate the clear presence of a relationship between  $T_p$  and  $M_s$  that significantly influences the simulation of welded-residual stresses in martensitic materials.

## 4. Conclusions

It was confirmed that for a TIG weld and in the condition of a thin plate, the approximation of a bi-dimensional Gaussian

heat source was satisfactory since it was able to correlate with high precision the thermal profile data obtained by the thermocouples and the numerical results.

From the Three-bar model, the effects of martensitic transformation were evident on the calculated final residual stresses, including the influence of  $T_p$  on  $M_s$  and, consequently, on the residual stresses.

From the Plate model, it was observed that the previously calibrated Gaussian heat source proved to be a good approximation and could be used without significant discrepancies in the thermal profile from thin plates. The effects of martensitic transformation, including the influence of  $T_p$  on  $M_s$ , were significant, mainly in the longitudinal direction.

The subdivision of the HAZ (composed model) and considering the influence of  $T_p$  on  $M_s$  resulted in differences that should be considered when simulating the welding of martensitic steels.

## 5. References

1. Kou S. *Welding metallurgy*. Hoboken: John Wiley & Sons; 2003.
2. Messler RW Jr. *Principles of welding: processes, physics, chemistry, and metallurgy*. Weinheim: John Wiley & Sons; 2008
3. Marques PV, Modenesi PJ, Bracarense AQ. *Soldagem-fundamentos e tecnologia*. Belo Horizonte: Editora UFMG; 2005.
4. Darmadi DB. Study of residual stress mechanism using three elasto-plastic bars model. *Asian Transaction*. 2011;1(5):76-80.
5. Porcaro RR, Araújo FC, Godefroid LB, Faria GL, Silva LL. Simulação do processo de soldagem elétrica por centelhamento de um aço para trilhos ferroviários. Parte 1: análise de tensões residuais via elementos finitos. *Soldag Insp*. 2019;24:e2412.
6. Deng D, Murakawa H. Prediction of welding distortion and residual stress in a thin plate butt-welded joint. *Comput Mater Sci*. 2008;43(2):353-65.
7. Marques ES, Silva FJ, Pereira AB. Comparison of finite element methods in fusion welding processes: a review. *Metals*. 2020;10(1):75.
8. Bhatti AA, Barsoum Z, Murakawa H, Barsoum I. Influence of thermo-mechanical material properties of different steel grades on welding residual stresses and angular distortion. *Mater Des*. 2015;65:878-89.
9. Francis JA, Stone HJ, Kundu S, Rogge RB, Bhadeshia HK, Withers PJ, et al. Transformation temperatures and welding residual stresses in ferritic steels. In: *ASME Pressure Vessels and Piping Conference*; 2007 July 22-26; San Antonio, USA. Proceedings. New York: ASME; 2007. p. 949-56.
10. Lee CH, Chang KH. Finite element simulation of the residual stresses in high strength carbon steel butt weld incorporating solid-state phase transformation. *Comput Mater Sci*. 2009;46(4):1014-22.
11. Lee CH, Chang KH. Prediction of residual stresses in high strength carbon steel pipe weld considering solid-state phase transformation effects. *Comput Struc*. 2011;89(1-2):256-65.
12. Souza SD, Moreira PS, Faria GL. Austenitizing temperature and cooling rate effects on the martensitic transformation in a microalloyed-steel. *Mater Res*. 2020;23(1):e20190570.
13. Deng D. FEM prediction of welding residual stress and distortion in carbon steel considering phase transformation effects. *Mater Des*. 2009;30(2):359-66.
14. Deng D, Murakawa H. Prediction of welding residual stress in multi-pass butt-welded modified 9Cr-1Mo steel pipe considering phase transformation effects. *Comput Mater Sci*. 2006;37(3):209-19.

15. Yaghi AH, Hyde TH, Becker AA, Sun W. Finite element simulation of welding and residual stresses in a P91 steel pipe incorporating solid-state phase transformation and post-weld heat treatment. *J Strain Anal Eng Des.* 2008;43(5):275-93.
16. Chen BQ, Hashemzadeh M, Guedes Soares C. Numerical and experimental studies on temperature and distortion patterns in butt-welded plates. *Int J Adv Manuf Technol.* 2014;72(5-8):1121-31.
17. Souza SS. Estudo da cinética de transformação martensítica em um aço microligado USISAR80T [master's thesis]. Ouro Preto: Rede Temática em Engenharia de Materiais, Universidade Federal de Ouro Preto; 2019.
18. Tsirkas SA, Papanikos P, Kermanidis T. Numerical simulation of the laser welding process in butt-joint specimens. *J Mater Process Technol.* 2003;134(1):59-69.
19. Hu Z, Zhao J. Effects of martensitic transformation on residual stress of P91 welded joint. *Mater Res Express.* 2018;5(9):096528.
20. Tavares TB, Porcaro RR, Cândido LC, de Faria GL, Dâmaso HV. Desenvolvimento de dispositivo de baixo custo para mecanização da soldagem GTAW e sua aplicação em estudo de solidificação de aço ABNT 430. *Tecnol Metal Mater Min.* 2020;17(1):13-22.
21. Gilles P, El-Ahmar W, Jullien JF. Robustness analyses of numerical simulation of fusion welding NeT-TG1 application: "Single weld-bead-on-plate". *Int J Press Vessels Piping.* 2009;86(1):3-12.
22. Knoedel P, Gkatzogiannis S, Ummenhofer T. Practical aspects of welding residual stress simulation. *J Construct Steel Res.* 2017;132:83-96.
23. Lindgren LE. Finite element modeling and simulation of welding part 1: increased complexity. *J Therm Stresses.* 2001;24(2):141-92.
24. Chen X, Fang Y, Li P, Yu Z, Wu X, Li D. Microstructure, residual stress and mechanical properties of a high strength steel weld using low transformation temperature welding wires. *Mater Des.* 2015;201(65):1214-21.
25. Lee CH. Computational modelling of the residual stress evolution due to solid-state phase transformation during welding. *Model Simul Mater Sci Eng.* 2008;16(7):075003.
26. Porcaro RR. Efeito da soldagem elétrica por centelhamento na microestrutura, propriedades mecânicas e resistência à fadiga de um aço para trilhos ferroviários: análise experimental e numérica [dissertation]. Ouro Preto: Rede Temática em Engenharia de Materiais, Universidade Federal de Ouro Preto; 2019.
27. Gedney BL, Rizos DC. Combining welding-induced residual stress with thermal and mechanical stress in continuous welded rail. *Results in Engineering.* 2022;16(2):100777.
28. Haibatollahi SP, Tehrani PH. Prediction of residual stress distribution in flash butt welded rails using electro-thermo-mechanical simulation. *Int J Veh Struct Syst.* 2013;5(1):53-7.
29. Araújo DB, Teixeira PR, Cunda LA. Applicability of the gaussian distribution heat source model to the thermal simulation of welding processes. In: 22nd International Congress of Mechanical Engineering; 2013 Nov 3-7; Ribeirão Preto, Brazil. *Proceedings. Rio de Janeiro: ACBM;* 2013. p. 10023-32.
30. Venkatkumar D, Ravindran D. Effect of boundary conditions on residual stresses and distortion in 316 stainless steel butt welded plate. *High-Temp Mater Process.* 2019;38(2019):827-36.
31. Malik MA, Qureshi ME, Dar NU. Numerical simulation of arc welding investigation of various process and heat source parameters. *Fail Eng Mater Struct.* 2007;30:127-42.
32. Heinze C, Pittner A, Rethmeier M, Babu SS. Dependency of martensite start temperature on prior austenite grain size and its influence on welding-induced residual stresses. *Comput Mater Sci.* 2013;69:251-60.